The structure of 3D collisional bow shocks in pulsed-power-driven plasma flows

R. Datta,[1] D. R. Russell,[2] I. Teng,[2] T. Clayson,[2] J. P. Chittenden,[2] S. V. Lebedev,[2] and J. D. Hare[1]
[1)] *Plasma Science and Fusion Center, Massachusetts Institute of Technology, Cambridge MA02139*
[2)] *Blackett Laboratory, Imperial College London, London SW7 2BW, United Kingdom*

(Dated: 6 July 2023)

We investigate 3D bow shocks in a highly collisional magnetized Aluminum plasma, generated during the ablation phase of an exploding wire array on the MAGPIE facility (1.4 MA, 250 ns). Ablation of plasma from the wire array generates radially diverging, supersonic ($5 < M_1 < 8$), super-Alfvénic magnetized flows with frozen-in magnetic flux ($Re_m \gg 1$). These flows collide with inductive probes placed in the flow, which serve both as the obstacles that generate the magnetized bow shocks, and as diagnostics of the advected magnetic field and flow velocity. Laser interferometry is used to diagnose the line-integrated electron density. A detached bow shock forms ahead of the probe and exhibits a fully 3D structure. The shock opening-angle is larger in the plane parallel to the magnetic field than in the plane perpendicular to the field. We calculate the the shock Mach angle from the shock geometry to determine the Mach number of the upstream flow. The Mach angles are $\sim$11° and $\sim$7° in the parallel and perpendicular planes respectively. The larger Mach angle in the plane parallel to the magnetic field lines indicates the presence of flux pile-up. Inductive probe measurements show that the peak post-shock magnetic field is $\sim$ 14 T. We determine the velocity of the flow from the time-of-flight of the plasma to the probe, and by combining this information with the observed shock geometry, we estimate the temperature of the plasma. The velocity and electron temperature are in good agreement with values reported from Thompson scattering measurements in similar flows. Finally, we compare the experimental results with fully 3D simulations performed using the resistive MHD code GORGON

I. INTRODUCTION

Large astrophysical objects often produce high Mach number flows which interact with ambient media, planetary obstacles, and/or spacecraft to generate strongly radiating shocks. Some examples include extrastellar jets from radio galaxies,[1–4] Herbig-Haro jets from young stellar objects (YSOs),[5–7] and shocks in core-collapse supernovae and supernova remnants[8–10]. Astrophysical flows can also exhibit dynamically significant magnetic fields, and shock formation in such systems is often accompanied by strong radiative cooling, hydrodynamic and magnetohydrodynamic (MHD) instabilities, and turbulence, which can significantly modify the shock dynamics.[11,12]

Laboratory astrophysics experiments at HEDP facilities have provided key insights into the physics of shocks in plasmas. HED laser plasmas have been used extensively to study physics relevant to astrophysical shocks, such as the evolution of hydrodynamic instabilities in shocks,[13,14] interaction of shocks and jets and with low-density ambient media,[15–17] and the formation of strongly radiating bow shocks.[18] Laser-driven plasmas are typically used to study shocks in collisionless plasmas with small magnetic fields.

In comparison, pulsed-power driven Z-pinch wire arrays provide an excellent platform to study magnetized shocks in the highly-collisional regime. Pulsed-power machines generate plasma by applying a large current to a load, typically an array of thin wires over a short period of time. The ablation of plasma from wire arrays produces highly collisional ($\lambda_{ii}/a \ll 1$), hypersonic and super-Alfvénic upstream flows with frozen-in magnetic flux ($Re_m \gg 1$).[19] Pulsed-power driven plasmas have been used extensively to study physics relevant to hypersonic astrophysical jets, such as the interaction of plasma jets with neutral gases,[20,21] the fragmentation of radiatively-cooled bow shocks in counter-propagating jets,[22] and the structure of radiatively-cooled oblique shocks,[23] planar shocks,[24] and quasi-2D bow shocks.[19,25,26]

Experiments show that the pile-up of magnetic flux modifies the structure of shocks generated by the interaction of super-fast plasma flows with stationary obstacles.[19,24,25] In quasi-2D bow shocks generated from the interaction of plasma with cylindrical obstacles, the structure of the bow shocks depends on the orientation of the advected magnetic field relative to the obstacle axis.[25] When the obstacle axis is perpendicular to the advected magnetic field, magnetic field lines accumulate and drape around the obstacle. The shape of the resulting bow shock is modified by the accumulated magnetic flux, and is determined by a competition between the upstream ram pressure and the magnetic tension of the bent field lines. This results in wide bow shocks with a large stand-off distance and opening angle.

In contrast, when the obstacle axis is parallel to the advected magnetic field, magnetic field lines slip past the obstacle and do not accumulate ahead of the obstacle. The result is a sharp bow shock with a smaller stand-off distance. For dielectric obstacles or conducting obstacles of small diameter, the bow shock structure resembles that of the parallel orientation, suggesting that magnetic field diffuses through the resistive obstacle faster than it can accumulate.[19,25] Although quasi-1D and quasi-2D shocks in magnetized plasmas have been examined extensively, full 3D shocks in magnetized pulsed-power plasmas have received less attention as they require careful diagnosis for proper interpretation.

In this paper, we show that bow shocks around small 3D obstacles in a supersonic ($M_S = v_{\rm flow}/C_S \sim 5$) and super-fast magnetosonic ($M_S = v_{\rm flow}/V_{MS} \sim 2$) plasma exhibit a fully 3D structure, with a larger shock opening angle in the plane parallel to magnetic field, than in the plane normal to the field.

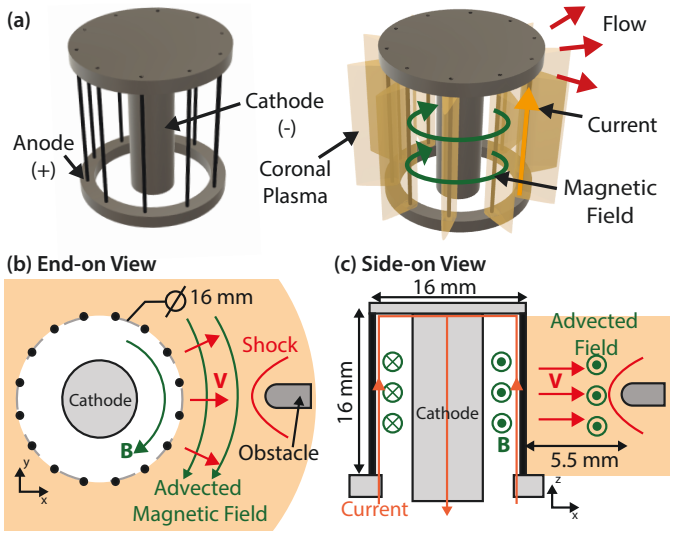

FIG. 1. (a) 3D representation of an exploding wire array (b) End-on (xy-plane) view of the experimental geometry, showing a cylindrical array of 16 equally-spaced 30 μm Al wires around a central cathode. An inductive probe serves as the obstacle and is placed ~ 5.5 mm from the array surface. (b) Side-on (xz-plane) view of the experimental geometry.

Even though the magnetic Reynolds' number of the upstream flow is expected to be large, the resistive diffusion length near the obstacle can be significant enough to decouple the magnetic field from the plasma, and create a hydrodynamic shock. The obstacles used in these experiments are inductive probes, which not only generate the shocks, but also measure the post-shock magnetic field. Even though inductive probes are widely used in HEDP experiments, their perturbative nature leads to questions about how reliably they can reconstruct the magnetic field in plasma flows. These experiments additionally aim to resolve this question by careful comparison between numerical simulations and experimental data. Finally, we also introduce a novel diagnostic technique based on simultaneous imaging of the bow shock and voltage measurements of the inductive probe, which allows us to estimate both the time-resolved velocity and temperature in the plasma flow.

II. EXPERIMENTAL AND DIAGNOSTIC SETUP

A. Load Hardware

The experimental setup is illustrated in Figure 1. The load consists of a cylindrical array of 16 equally-spaced 30 μm diameter aluminum wires (California Wire Company) around a central 5 mm diameter stainless steel cathode. The array diameter and the array height are both 16 mm. The load is placed within a vacuum chamber that sits atop the magnetically insulated transmission Line (MITL) of the pulsed-power generator. The current pulse (1.4 MA peak current, 250 ns rise time) is generated using the MAGPIE generator at Imperial College London.[27]

When current flows through the wires, the wires heat up resistively. The wire material vaporizes and ionizes to create a ring of low-density coronal plasma around the dense wire cores. Current density is mostly concentrated within a thin skin region containing the coronal plasma immediately around the stationary wire cores, and the global magnetic field points azimuthally inside the array, and rapidly drops to zero outside the array.[28] The global $\mathbf{j} \times \mathbf{B}$ force accelerates the coronal plasma radially outwards, and the ablating plasma streams supersonically into the flow region around the array. We can calculate the magnetic field inside the array using Ampere's law $B_\theta = \mu_0 I/2\pi r$ — for our array geometry, the maximum driving magnetic field strength at the array surface is expected to be $B_{\max} = 35$ T. The ion-ion mean free path of the ablating plasma is typically small ($\lambda_{ii} \sim 10^{-3}$mm), and the magnetic Reynolds number is typically large $Re_m \sim 10 - 100$.[19] The ablating plasma advects some of the current density and the magnetic field at the array surface radially outwards, resulting in outflows of highly collisional magnetized plasma. The velocity of the ablating plasma in similar setups is typically supersonic ($M_S \sim 5$), super-Alfvénic ($M_A \sim 2$) and super-fast magnetosonic ($M_f \sim 2$),[19,25] and the adiabatic index of the plasma (ratio of specific heats) is typically lower than that of an ideal gas $\gamma \sim 1.1 - 1.2$.[23,29] When these hypersonic outflows collide with the obstacles, they generate detached bow shocks.

In contrast to previous experimental work, an inductive probe serves as the obstacle, and is placed ~ 5.5 mm from the array surface. In addition to generating bow shocks, the probe also measures the post-shock magnetic field.

B. Diagnostic Setup

The probe placed in the flow consists of two strands of oppositely-wound single-turn enamel-coated copper wire, threaded through a ~ 1 mm diameter thin steel tube. The voltage response of the probe can have two contributions — one due to the time-varying magnetic flux through the loop, and another electrostatic component due to the coupling of stray voltages, or the voltage from the pulsed-power generator. Having two oppositely-wound loops in the inductive probe provides a differential measurement, allowing us to combine the signals from each loop and isolate the contribution of the time-varying magnetic flux .

We position the inductive probe to measure the azimuthal magnetic field (with respect to the array center); the normals to the surfaces of the loops lie along the magnetic field. The inductive probe was calibrated before use in the experiment to determine the effective area A_p of the probe. This was done by placing the probe within the known magnetic field generated by a ~ 1 kA time-varying current. The effective area of the probe determined from the calibration is $A_{\text{eff}} = 0.295 \pm 0.01\,\text{mm}^2$. The voltage signal from the probe is proportional to the time-rate of change of the magnetic field $V = \dot{B}A_p$.[30] To determine the magnetic field strength at the probe, we numerically integrate the signal in time.

In addition to the inductive probe placed in the flow, a sec-

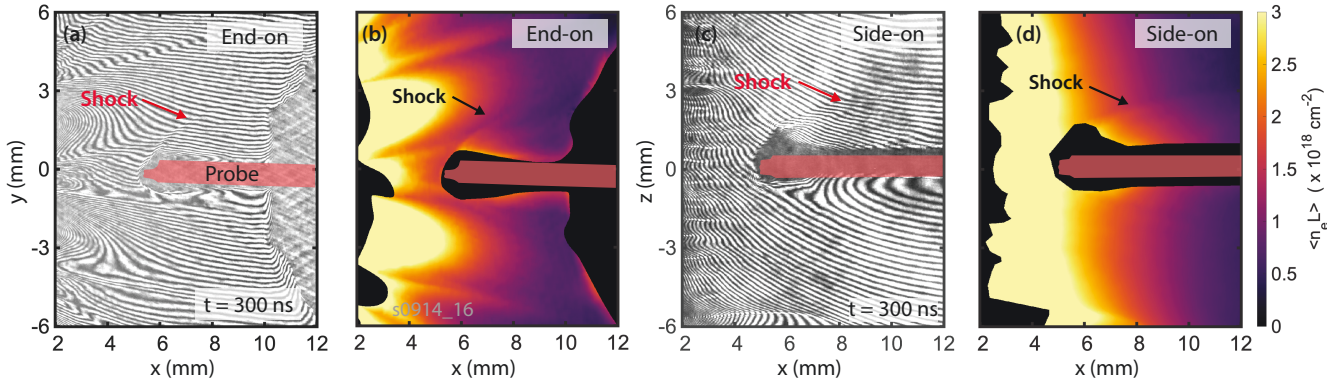

FIG. 2. (a) End-on raw interferogram at 300 ns after current start using a Mach-Zehnder interferometer with a 532 nm laser. The red shaded region represents the silhouette of the obstacle from the background interferogram at t = 0. (b) End-on line-integrated electron density map determined from interferometry. (c) Side-on raw interferogram at 300 ns after current start using a 1053 nm laser. (d) Side-on line-integrated electron density map determined from interferometry. A detached bow shock is visible ahead of the probe in both side-on and end-on views. The shock opening half-angle is larger in the end-on view than in the side-on view. Regions in black near the obstacle and the wire array surface represent locations where the probing beam is lost.

ond inductive probe is placed in a recess inside the MITL of the pulsed-power machine, and is used to monitor the current in the load. The signal from the probes is recorded using an oscilloscope with a 1 ns digitization rate.

We use a Mach-Zehnder interferometry system to visualize the plasma flow and to determine the line-integrated electron density. Our interferometry system is set up to provide both end-on and side-on views of the experimental setup. The end-on (x-y plane) view, which provides an axially integrated view of the experimental setup, is illuminated using a 532 nm pulsed Nd-YAG laser (EKSPLA SL321P, 500 ps, 500 mJ). The side-on view provides a line-integrated (along the y-direction) view of the x-z plane. It is illuminated using a 1053 nm Nd:Glass laser (1 ns, 5 J). We use a coordinate system centered at the interaction of the obstacle axis and the array surface throughout this paper. Note that the magnetic field lines lie parallel to the end-on plane, and normal to the side-on plane.

We combine the probe beam (which passes through the plasma) and the reference beam (which passes through air/vacuum) at the CCD of a Canon 350D DSLR camera. The probe and reference beams are slightly misaligned to generate a spatially-heterodyned system. In the absence of plasma, this creates a linear pattern of bright and dark interference fringes. When the probe beam propagates through the laser, the resulting phase accumulated by the beam (which is proportional to the path-integrated electron density along the beam) distorts the fringe pattern and introduces a spatially-varying fringe shift.[23,30] We use the observed fringe shift to reconstruct the phase difference between the probe and reference beams, and to calculate the line-integrated electron density.[31]

III. RESULTS

A. Bow Shock Morphology

Figure 2 shows the end-on and side-on raw interferograms, and the processed line-integrated electron density maps at 300 ns after current start. A detached bow shock, characterized by a curved discontinuity in electron density, is visible in both end-on and side-on images. Note that the bow shock is more distinct on the top of the probe in both end-on and side-on images, because the shock front is almost parallel to the fringes under the probe, so the fringes appear relatively undisturbed. The shock front appears distinct on the other side of the probe, where the fringes are at an angle to the shock. Nevertheless, we expect the shock front to be axisymmetric about the obstacle axis, due to the symmetry of the upstream flow.

In both end-on and side-on images, the electron density is high near the surface of the wire array and decreases with distance from the array. In the end-on plane, the upstream flow exhibits significant modulation in the azimuthal direction. The azimuthal modulation results from the supersonic collision of adjacent jets emanating from the wire cores, which form hot dense standing oblique shocks.[23] Due to the oblique shocks, we expect the Mach number of the upstream flow in the end-on plane to also exhibit some modulation. In comparison, the upstream flow in the side-on plane is relatively more uniform. Regions in black near the obstacle and the wire array surface represent locations where the probing beam is lost due to shadowgraphy or critical density effects.

We define the shock opening half-angle $\alpha/2$ as the angle between the obstacle axis and the shock front (see Figure 3). The opening half-angle decreases continuously with distance from the nose of the obstacle. From Figure 2, we see that the shock opening angle is larger in the end-on plane than in the side-on plane. We define the shock angle σ as the angle between the upstream velocity vector and the shock front (Fig-

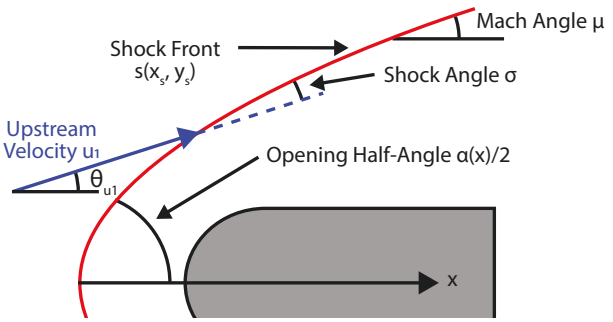

FIG. 3. Schematic showing bow shock geometry observed ahead of the inductive probe in the end-on view. The shock front is represented by the red solid line. The opening half-angle is the angle between the obstacle axis and the shock front. The shock angle is the angle between the upstream velocity and the shock front.

ure 3). If the upstream velocity vector $\mathbf{u_1}$ makes an angle θ_{u1} with respect to the horizontal, we can determine the shock angle from the opening half-angle and the velocity angle using $\sigma = \alpha/2 - \theta_{u1}$. To determine the opening-half angle from the observed bow shock geometry, we trace the shock front and fit a curve $s(x_s, y_s)$ to it. The opening half-angle then becomes $\alpha(x_s)/2 = \tan^{-1}(dy_s/dx_s)$.

What is the value of the upstream velocity angle θ_{u1}? In the side-on plane, the upstream velocity only has a component along the x-direction, i.e. $\theta_{u1} = 0$. So the opening half-angle and the shock angle are equal in the side-on view. In the end-on view, the velocity vector makes a non-zero angle with the horizontal due to the radially diverging nature of the flow. Therefore, we must account for the direction of the upstream velocity when calculating the shock angle. We assume that the upstream velocity propagates radially outwards with respect to the array center. The upstream velocity then makes an angle $\theta_{u1} = \tan^{-1}(y_s/x_s)$ to the horizontal.

In a bow shock, the shock angle varies continuously from 90° at the nose of the obstacle to the Mach angle μ asymptotically far away from the obstacle, where the bow shock constitutes an infinitesimally weak Mach wave.[32] From our interferometry images (Figure 2), we observe that the shock opening half-angle approaches $\alpha/2 \rightarrow 30°$ and $\alpha/2 \rightarrow 7°$ far away from the obstacle in the end-on and side-on views respectively. Accounting for the direction of the upstream velocity, the Mach angles are $\mu \approx 11 \pm 0.5°$ and $\mu \approx 7 \pm 0.5°$ in the end-on and side-on planes respectively. The Mach angle is $\approx 3°$ higher in the end-on plane. We discuss the difference between the end-on and side-on Mach angles in §IV.

The structure of shocks is closely related to the propagation velocity of linear perturbations in a given medium.[33,34] If we assume that the linear wave phase velocity in the plasma is isotropic, we can use the simple relation $\sin\mu = 1/M_1$ to obtain the upstream Mach number.[34] From the Mach angle measured in the end-on plane, we estimate the upstream Mach number to be $M_1 = 5.2 \pm 0.3$. In the side-on plane, the upstream Mach number is $M_1 = 8.2 \pm 0.6$.

The assumption of an isotropic linear phase velocity requires further elaboration. If the shock is hydrodynamic, then the sound wave, which propagates isotropically at the ion sound speed C_s, sets the Mach angle.[33] In a fast magnetohydrodynamic shock, the fast magnetosonic wave which determines the shock dynamics exhibits an anisotropic phase velocity — the fast wave propagates at the magnetosonic velocity $\sqrt{V_A^2 + C_S^2}$ perpendicular to the magnetic field, and at the higher of the sound speed and Alfvén speed V_A parallel to the magnetic field[33]. The anisotropy in the fast wave phase velocity is small in the high β ($V_f \approx C_S$) and low β ($V_f \approx V_A$) regimes. Experimental results from pulsed-power aluminum plasmas in similar exploding wire arrays have shown that the magnetic pressure dominates, so that the Alfvén speed V_A exceeds the sound speed C_S.[23,25,35] Furthermore, similar experiments with 2D cylindrical obstacles show that the fast and Alfvén Mach numbers are expected to be roughly ~ 2 (while the sound Mach number $M_S > 5$).[19,25] This indicates that the fast magntosonic speed V_f is approximately equal the Alfven speed V_A (β is small), and we can expect the anisotropy in the fast wave speed to be small. The expected value of the upstream Mach number determined from the shock geometry ($M_S \sim 5 - 8$) is in close agreement with the sonic Mach number observed in similar aluminum puled-power plasmas, which suggests that the observed bow shock is hydrodynamic-like, and the magnetic field plays a limited role in the shock dynamics.

Why is the bow shock hydrodynamic? The ideal MHD Rankene-Hughniot shock jump conditions reduce to those of a hydrodynamic jump when the upstream magnetic field is parallel to the shock normal.[33] However, this is not the case for our geometry. The upstream magnetic field, which points in the azimuthal direction, always forms some angle to the shock front. In fact, at the nose of the obstacle, the angle between the shock normal and the upstream field will be 90°, which constitutes a strong perpendicular MHD shock, that leads to equal compression ratios for the density and magnetic field.[33] The other limit in which an ideal MHD shock becomes hydrodynamic is the large β limit ($B \rightarrow 0$), where the thermal pressure of the plasma dominates over the magnetic pressure. Again, for pulsed-power driven aluminum plasmas, the magnetic field is typically dynamically significant $\beta \sim 0.1 - 1$, so this also doesn't explain the hydrodynamic nature of the shock. In resistive MHD, however, resistivity breaks the frozen-in condition of ideal MHD, and the magnetic field may diffuse independently of the plasma velocity. The decoupling of the plasma and magnetic field occurs at a length scale which makes the magnetic Reynolds' of order unity, i.e. $Re_m = UL/\bar{\eta} \sim 1$. Here, $\bar{\eta}$ is resistive diffusivity η/μ_0 of the plasma. Diffusion dominates, and the magnetic field becomes poorly coupled to the plasma at length scales smaller than the resitive diffusion length scale L_η, which may explain the non-MHD nature of the observed bow shock.

B. Magnetic Field, Velocity, and Temperature Measurements

Figure 4a shows the voltage signal from the inductive probes placed near the MITL (henceforth, referred to as the

load probe) and in the flow. The signal from load probe is proportional to the time rate of change of the current in the wire array, and exhibits a characteristic 'double-bumped' structure with a larger peak at $\sim$ 85 ns and a smaller peak at $\sim$ 180 ns, caused by reflections from impedance mismatches within the transmission lines.[27] The rise time of the load current is $\sim$ 250 ns. Due to a lack of calibration information we only show the shape of the current waveform rather than its magnitude. Other experiments show that MAGPIE consistently delivers a 1.4 MA peak current, which what we used in the later simulations of this experiment.[24,25,31,36,37] The probe in the flow approximately reproduces the shape and characteristic features of signal at the MITL, including the characteristic 'double bump', showing that the magnetic field is frozen into the flow, and that the magnetic field from the inside of the array is advected to the outside by the ablating plasma.

Figure 4b shows the normalized load current and the advected post-shock magnetic field. The normalized load current is determined by numerically integrating the load inductive probe signal. The advected magnetic field is determined by integrating the voltage signals from the probe in the flow. The load current and the advected magnetic field have similar shapes, again confirming that the magnetic flux is frozen into the flow. We calculate a post-shock peak magnetic field of $\sim$ 14 T.

We determine the velocity of the plasma at the inductive probe from the ratio of the distance between the probe and array surface, to the time-of-flight of the plasma to the probe (Figure 4c). We measure the time-of-flight from the time interval between the corresponding features on the load and the probe signals respectively (represented by the circles in Figure 4a). The distance to the probe (L = 5.55 $\pm$ 0.25 mm) is determined from the interferometry images. The velocity at the probe is $\sim$ 100 km s^{-1} early in time and decreases to $\sim$ 60 km s^{-1} at $t \approx 350$ ns. We compare the flow velocity determined from time-of-flight data with the flow speed determined in similar exploding arrays using Thompson scattering, and find that the flow velocity calculated using this method is in good agreement with that reported in literature.[24,25]

At 300 ns, the velocity at the probe is $62 \pm 12\,\mathrm{km\,s^{-1}}$. From the interferometry images, we know that the expected upstream Mach numbers are 5.2 ± 0.3 and 8.2 ± 0.6 in the end-on and side-on planes respectively. If we assume that the shock is hydrodynamic, then we can determine the average sound speed C_S and electron temperature ZT_e of the plasma. Using these values, the average sound speed becomes $C_S = 11.8 \pm 2.4$ km s^{-1} from the end-on plane measurements, and $C_S = 7.6 \pm 1.6$ km s^{-1} from the side-on plane measurements. This corresponds to $ZT_e = 35 \pm 14$ eV and $ZT_e = 14 \pm 6$ eV in the end-on and side-on planes respectively. For comparison, the value of ZT_e determined using Thomson scattering in a similar pulsed-power driven Aluminum plasma is $\sim$ 42 eV.[25] Assuming an average ionization of 3.5 for the aluminum plasma, the expected electron temperature is $T_e \approx 10$ eV (end-on) and $T_e \approx 4$ eV (side-on).

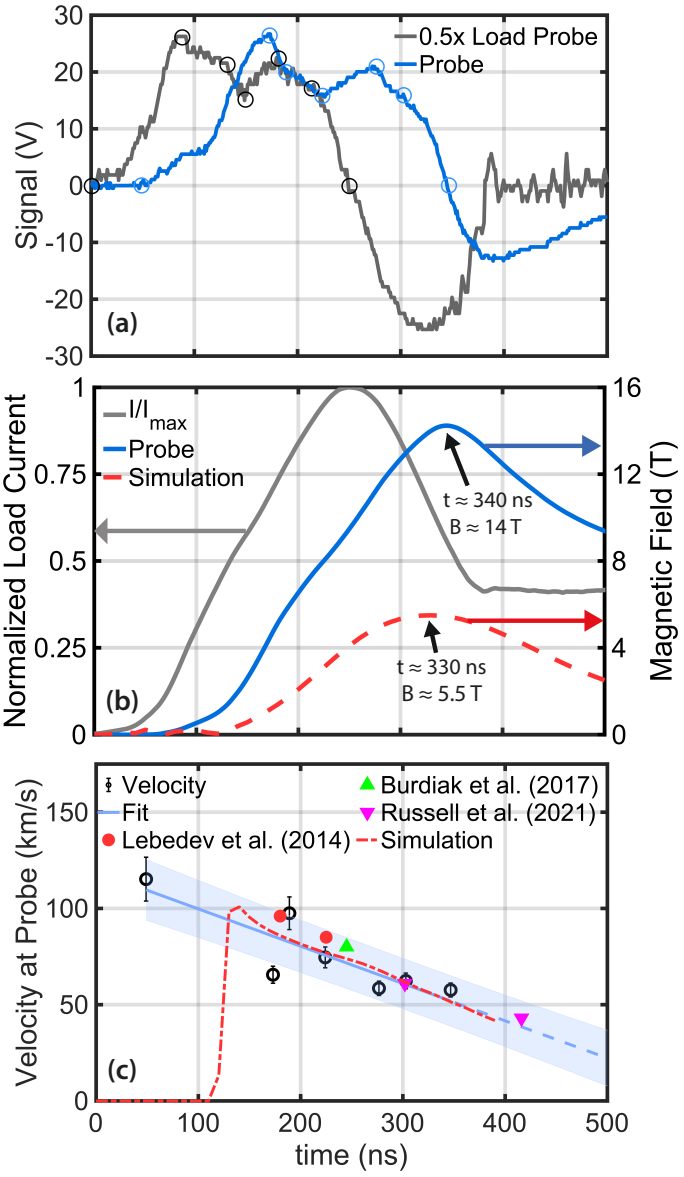

FIG. 4. (a) Signal from load probe and inductive probe placed in the flow. Both signals have similar shapes and are displaced in time, showing that the magnetic field is frozen into the flow. (b) Time-resolved load current and magnetic field. Peak field value is $\sim$ 14 T and occurs at $\sim$ 340 ns after current start. (c) Time-resolved velocity measurements at the probe location. Velocity is $\sim 100\,\mathrm{km\,s^{-1}}$ early in time and decreases to $\sim 60\,\mathrm{km\,s^{-1}}$ at $\sim$ 350 ns.

IV. DISCUSSION AND COMPARISON WITH SIMULATIONS

We perform full 3D simulations of a 16 mm diameter 16 mm tall exploding wire array with 16 equally-spaced 30 µm aluminum wires. A sine-squared current profile ($I_{pk} = 1.4$ MA, $t_{\mathrm{rise}} = 240$ ns) was applied to the load. The simulation domain is a cuboid with dimensions $60 \times 60 \times 45$ mm^3, and resolution $\approx 180\,\mu$m. The wire core diameter is set to $\approx 540\,\mu$m. We place a resistive cylindrical obstacle of radius

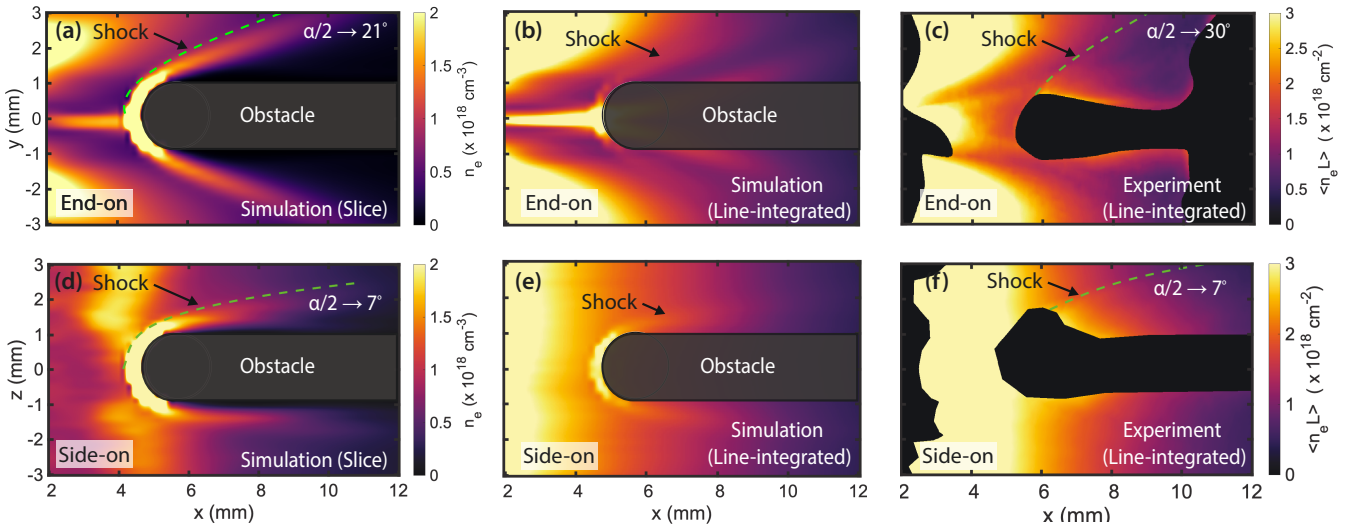

FIG. 5. (a) End-on slice of electron density at 300 ns from 3D resistive MHD GORGON simulation of the experimental geometry. (b) End-on line-integrated electron density at 300 ns from 3D resistive MHD GORGON simulation of the experimental geometry. (c) Experimental end-on line-integrated electron density at 300 ns from plasma interferometry (reproduced here from Figure 2). In each image, the plasma flow is from the left to the right, and the magnetic field lies in the plane of the page. A bow shock, characterized by a discontinuous increase in electron density, is visible ahead of the obstacle. Far from the obstacle, the opening half-angle in the end-on plane approaches $\approx 21^o$ in the simulation, and $\approx 30^o$ in the experiment.

$\sim$ 1 mm at 5.5 mm from the array surface. The cylindrical obstacle mimics the inductive B-dot probes in the experiment, and is aligned parallel to the x-axis. The leading edge of the cylinder is a non-conducting sphere of radius $\sim$ 1 mm. The obstacle is positioned such that the oblique shock centerline is parallel to the obstacle axis.

Figure 5a and Figure 5d show the end-on and side-on slices of the simulated electron density through the obstacle mid-plane at 300 ns, and Figure 5b and 5d show the end-on and side-on line-integrated electron density at 300 ns. A detached bow shock is visible ahead of the obstacle in both the electron density slices and the line-integrated maps. In the line-integrated electron density maps, the shock front appears 'muted', similar to what we observe in the experimental image, because line-integrating obfuscates the intensity of the 3D shock front.

The simulated upstream flow is qualitatively similar to the experimentally observed flow. The electron density is higher closer to the array surface and decreases with distance from the array in both the simulation and experiment. In the end-on plane, the upstream flow in both the simulated and experimentally observed electron density maps are modulated in the azimuthal direction due to the formation of oblique shocks between adjacent plasma jets, while in the side-on plane, the upstream flow is relatively more uniform. The opening half-angle in the end-on plane is larger than in the side-on plane, similar to what is observed in the experiment. Far from the obstacle, the opening half-angle in the side-on plane approaches $\sim 7^\circ$ in both the simulation and experiment. In the end-on plane, however, the opening half-angle in the end-on plane approaches $\sim 21^\circ$ in the simulation, and $\sim 30^\circ$ in the experiment. We determine the shock angle in the simulation by subtracting the angle the upstream velocity makes with the horizontal from the opening half-angle. The Mach angles from the simulation are $\mu \approx 8^\circ$ in the end-on plane, and $\mu \approx 7^\circ$ in the side-on plane. This corresponds to an upstream Mach number of $7.2 < M_1 < 8.2$.

We can compare these values of the upstream Mach number obtained from shock geometry with those obtained from the simulated fluid properties. We calculate the sonic Mach number $M_S = u_1/C_S$. Here, $C_S = \sqrt{\gamma Z T_e/m_i}$ is the ion sound speed, Z is the ionization of the plasma, T_e is the electron temperature, and m_i is the ion mass. The adibatic index of the simulated plasma remains relatively constant at $\gamma \approx 1.13$ throughout the plasma. In the end-on plane, the sound Mach number is modulated between the oblique shocks and the jets, and varies between $4.8 < M_S < 8.2$ upstream of the shock. In the side-on plane, the upstream Mach increases with distance form the array, and varies between $4.8 < M_S < 6.9$ upstream of the shock. This range of sonic Mach numbers is in good agreement with the range of Mach numbers expected from the geometry of the simulated shock ($7.2 < M_1 < 8.2$), again confirming that simulated shock is hydrodynamic-like.

We also compute the fast Mach number $M_f = u_1/V_f$ of the flow. Note that the fast magnetosonic speed is assumed to be $V_f = \sqrt{C_S^2 + V_A^2}$. The plasma beta of the simulated plasma is $\beta \sim 0.1$, so the upstream fast phase velocity is roughly isotropic and the Mach number is approximately equal to the Alfvén Mach number. In the end-on and side-on views, the upstream flow is sub-fast just upstream of the obstacle, and the fast Mach number upstream of the shock increases to 1.1-1.9 away from the obstacle.

The upstream Mach number predicted from shock geome-

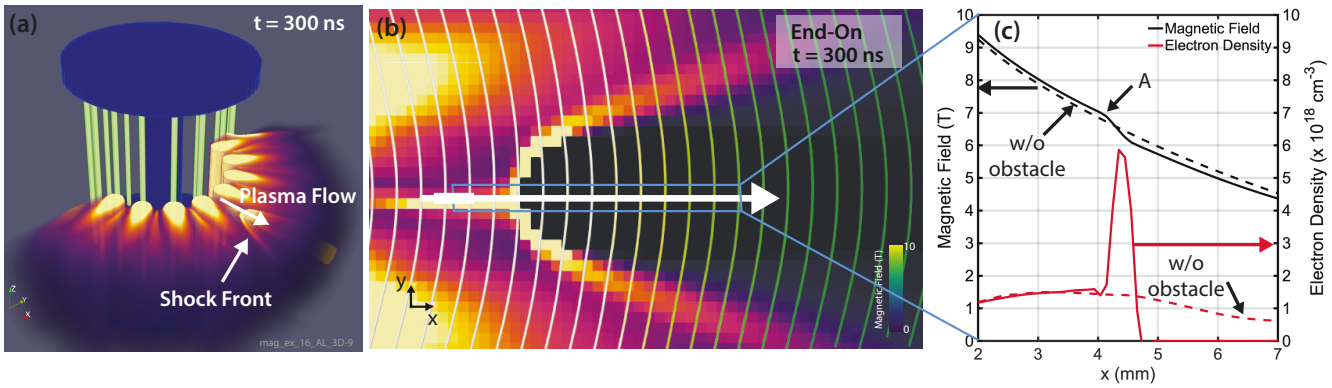

FIG. 6. (a) GORGON resistive MHD simulation with an electron density slice of the ablating plasma at 300 ns. A detached bow shock is seen ahead of the obstacle. The left half of the electron density slice is clipped for clarity. (b) Magnetic field lines overlaid on the electron density map generated in GORGON at 300 ns after current start. The magnetic field lines point in the azimuthal direction, and remain mostly unaffected by the shock front, confirming the hydrodynamic nature of the shock. (c) Line-outs of the magnetic field and electron density along the obstacle-axis. The magnetic field exhibits a negligible perturbation at the shock front (Position A).

try is in better agreement with the calculated upstream sonic Mach number M_S than with the fast Mach number M_f. This suggests that the simulated shock is hydrodynamic in nature, and that the magnetic field is able to diffuse resistively through the obstacle rather than be compressed ahead of it. We plot the magnetic field lines overlaid onto the simulated electron density map in Figure 6a. The magnetic field lines point in the azimuthal direction, and remain mostly unaffected by the shock front, confirming the hydrodynamic nature of the shock. 6b shows line-outs of the magnetic field and electron density along the obstacle axis. The magnetic field exhibits a negligible perturbation at the shock front. This can happen if the resistive diffusion length scale is large, such that the magnetic field decouples from the fluid, and diffuses through the obstacle, instead of piling-up, or being compressed by the shock. The calculated resistive diffusion length from the simulation is $L_\eta \sim 1$ cm. Furthermore, numerical resistivity, introduced due to a finite grid size, can also increase the resistive diffusion length scale.

In the simulation, where the shock is hydrodynamic, the end-on and side-on Mach angles are roughly similar, i.e. there is no anisotropy in the Mach angle. In the experiment, however, the Mach angle ($\sim 11°$) is higher in the end-on plane compared to the side-on plane ($\sim 7°$), which suggests that the magnetic field may introduce some anisotropy into the shock structure. As mentioned before, when magnetic field lines frozen into the flow approach an obstacle, they may pile-up ahead of the obstacle, slip past it, or diffuse through the obstacle (including the thin layer of dense hot stagnated plasma on the obstacle surface). If the rates of advective slipping and diffusion are small, then the magnetic field will drape around the obstacle, and the magnetic tension of the bent field lines will provide an additional force opposing the ram pressure of the incoming upstream flow. This will result in a larger opening angle and stand-off distance of the shock.[25] The end-on plane represents the plane parallel to the field lines, and this bending and larger opening angle should increase the end-on opening angle. However, in the side-on plane, the magnetic field lines are normal to the plane, so even when the magnetic field lines pile up, the bending of field lines does not affect the side-on shock angle. Therefore, we expect magnetic draping to modify the shock geometry only in the end-on plane and not on the side-on plane, unless the magnetic field pile-up is significant enough to change the upstream Mach number and plasma compressibility. The accumulation of the magnetic field will depend on the competition between the rates of pile-up, diffusion and slipping.

We can reduce the effect of finite numerical diffusivity in the simulations by increasing the spatial resolution. We simulate a subset of the computational domain with 4 wires that generate a quasi-planar upstream flow. These simulations show increased magnetic field pile-up ahead of the obstacle, and a larger Mach angle in the end-on plane than in the side-on plane. Increasing the conductivity of the obstacle also increases the magnetic field pile-up.

The peak simulated field at the probe (~ 5.5 T) is weaker than the experimentally observed peak field (~ 14 T) (Figure 4b). Although the magnetic field measured by the probe may be enhanced by flux pile-up, pile-up in this geometry is not expected to be significant enough to cause a ~ 3x change in the magnetic field. This suggests that the simulation may not completely capture the dynamics of shock formation in the plasma. In general, the simulation may underestimate the magnetic field advected from the inside of the array compared to the experiment. The advection of magnetic field by the coronal plasma around the wire cores can depend on complicated ablation dynamics, and include other physics, which resistive MHD codes do not account for.

V. CONCLUSIONS

We have presented experimental results and discussion of bow shocks generated in a collisional magnetized plasma due to collision of a supersonic super-fast flow with inductive probes. Interferometry images taken at 300 ns after current

start show a well-defined detached bow shock ahead of the probe. The bow shock has a fully 3D structure, with a larger opening angle in the end-on plane than in the side-on plane. Part of this effect is due to the radially diverging nature of the upstream flow. Assuming that the upstream flow points radially outwards from the array center, we subtract the angle of the velocity vector relative to the horizontal from the shock opening half-angle to determine the shock angle and Mach angles. From the shock geometry, the Mach angle is $11°\pm0.5°$ in the end-on plane, and $7°\pm0.5°$ in the side-on plane. These correspond to upstream Mach numbers of 5.2 ± 0.3 (end-on) and 8.2 ± 0.6 (side-on). The calculated Mach numbers are in good agreement with sonic Mach numbers reported in literature for similar aluminum plasmas, suggesting the shock is hydrodynamic. This may occur if the resistive diffusion length is large, such diffusion of magnetic field dominates over convection, and the frozen-in condition of ideal MHD is broken. The larger Mach angle in the end-on plane may suggest magnetic flux pile-up ahead of the probe. Magnetic field lines lie parallel to the end-on plane, and in this plane the draping of magnetic field lines will result in a wider shock opening angle, as the magnetic tension of the bent field lines opposes the incoming ram pressure. The magnetic field lines lie normal to the side-on plane, and any bending of the field lines will not be affect the shock opening angle when viewed in this plane.

Inductive probe measurements show good agreement between the shape of the signal at the load and in the flow, showing that the magnetic field is frozen into the flow. The peak magnetic field strength is 14 T and occurs at ~ 345 ns after current start. We use the time-of-flight of the plasma to the probe to estimate the flow velocity. The calculated flow velocity is consistent with the flow velocity of $50-100\,\mathrm{km\,s^{-1}}$ reported in literature for pulsed-power driven aluminum plasmas.

We compare our results with full 3D resistive MHD simulation in GORGON. The simulation successfully reproduces several features of the experiment, including a larger opening angle in the end-on plane than in the side-on plane. The Mach angle is side-on plane is 7°, which is in good agreement with the experimentally observed value. The Mach angle is end-on plane is 8°, which is ≈ 3 ° lower than the experimental value. This may be because the simulation may not be accurately capturing the magnetic field- pile-up ahead of the obstacle due to a dynamically significant resistive diffusion length. The upstream sonic Mach number calculated form the plasma parameters is in good agreement with the range of upstream Mach numbers expected from the shock geometry, showing that the simulation predicts a hydrodynamic shock.

The results presented here provide insight into the physics of 3D magnetized bow shocks, which are of relevance to many astrophysical plasma flows. Furthermore, we use a new diagnostic technique to estimate both the time-resolved velocity and temperature of the plasma, by simultaneously measuring the time of flight of the plasma to the inductive probe, and the geometry of the bow shock.

VI. ACKNOWLEDGEMENTS

The simulations presented in this paper were performed on the MIT-PSFC partition of the Engaging cluster at the MGHPCC facility (www.mghpcc.org) which was funded by DoE grant number DE-FG02-91-ER54109.

[1] G. Miley, "The Structure of Extended Extragalactic Sources," , 165–218 (1980).
[2] M. Smith and C. Norman, "Extrastellar Jets - Trajectories," Royal Astronomical Society , 148–162 (1981).
[3] G. C. Duncan and P. A. Hughes, "Simulations of relativistic extragalactic jets," The Astrophysical Journal **436**, L119 (1994), arXiv:9406041 [astro-ph].
[4] E. Choi, P. J. Wiita, and D. Ryu, "Hydrodynamic Interactions of Relativistic Extragalactic Jets with Dense Clouds," The Astrophysical Journal **655**, 769–780 (2007).
[5] P. Hartigan, J. Raymond, and J. Meaburn, "Observations and shock models of the jet and Herbig-Haro objects HH 46/47," The Astrophysical Journal **362**, 624 (1990).
[6] M. D. Smith, T. Khanzadyan, and C. J. Davis, "Anatomy of the Herbig – Haro object HH7 bow shock," Royal Astronomical Society **536**, 524–536 (2003).
[7] M. D. Smith, *Astrophysical Jets and Beams* (2012).
[8] D. Arnett and W. Arnett, *Supernovae and Nucleosynthesis: An Investigation of the History of Matter, from the Big Bang to the Present*, Princeton Series in Astrophysics (Princeton University Press, 1996).
[9] K. Kifonidis, T. Plewa, H.-T. Janka, and E. Müller, "Non-spherical core collapse supernovae," Astronomy Astrophysics **408**, 621–649 (2003).
[10] R. A. Chevalier, "Are young supernova remnants interacting with circumstellar gas," The Astrophysical Journal **259**, L85 (1982).
[11] B. A. Remington, R. P. Drake, and D. D. Ryutov, "Experimental astrophysics with high power lasers and Z pinches," Reviews of Modern Physics **78**, 755–807 (2006).
[12] S. V. Lebedev, A. Frank, and D. D. Ryutov, "Exploring astrophysics-relevant magnetohydrodynamics with pulsed-power laboratory facilities," Reviews of Modern Physics **91**, 25002 (2019).
[13] B. A. Remington, J. Kane, R. P. Drake, S. G. Glendinning, K. Estabrook, R. London, J. Castor, R. J. Wallace, D. Arnett, E. Liang, R. McCray, A. Rubenchik, and B. Fryxell, "Supernova hydrodynamics experiments on the Nova laser," Physics of Plasmas **4**, 1994–2003 (1997).
[14] J. Kane, D. Arnett, B. A. Remington, S. G. Glendinning, G. Bazan, R. P. Drake, B. A. Fryxell, R. Teyssier, and K. Moore, "Scaling supernova hydrodynamics to the laboratory," Physics of Plasmas **6**, 2065–2071 (1999).
[15] R. P. Drake, S. G. Glendinning, K. Estabrook, B. A. Remington, R. McCray, R. J. Wallace, L. J. Suter, T. B. Smith, J. J. Carroll, R. A. London, and E. Liang, "Observation of forward shocks and stagnated ejecta driven by high-energy-density plasma flow," Physical Review Letters **81**, 2068–2071 (1998).
[16] H. F. Robey, T. S. Perry, R. I. Klein, J. O. Kane, J. A. Greenough, and T. R. Boehly, "Experimental investigation of the three-dimensional interaction of a strong shock with a spherical density inhomogeneity," Physical Review Letters **89**, 085001/1–085001/4 (2002).
[17] J. M. Foster, B. H. Wilde, P. A. Rosen, R. J. R. Williams, B. E. Blue, R. F. Coker, R. P. Drake, A. Frank, P. A. Keiter, A. M. Khokhlov, J. P. Knauer, and T. S. Perry, "High-Energy-Density Laboratory Astrophysics Studies of Jets and Bow Shocks," The Astrophysical Journal **634**, L77–L80 (2005).
[18] A. Liao, P. Hartigan, G. Fiksel, B. Blue, P. Graham, J. Foster, and C. Kuranz, "Using the ROSS optical streak camera as a tool to understand laboratory experiments of laser-driven magnetized shock waves," **6**, 6–11 (2018).
[19] L. G. Suttle, G. C. Burdiak, C. L. Cheung, T. Clayson, J. W. D. Halliday, J. D. Hare, S. Rusli, D. R. Russell, E. R. Tubman, A. Ciardi, N. F. Loureiro, J. Li, A. Frank, and S. V. Lebedev, "Interactions of magnetized plasma flows in pulsed-power driven experiments," Plasma Physics and Controlled Fusion **62**, 014020 (2019).
[20] F. Suzuki-Vidal, S. V. Lebedev, M. Krishnan, M. Bocchi, J. Skidmore, G. Swadling, A. J. Harvey-Thompson, G. Burdiak, P. De Grouchy, L. Pickworth, L. Suttle, S. N. Bland, J. P. Chittenden, G. N. Hall, E. Khoory, K. Wilson-Elliot, R. E. Madden, A. Ciardi, and A. Frank, "Laboratory

astrophysics experiments studying hydrodynamic and magnetically-driven plasma jets," Journal of Physics: Conference Series **370** (2012).

[21]F. Suzuki-Vidal, S. V. Lebedev, M. Krishnan, J. Skidmore, G. F. Swadling, M. Bocchi, A. J. Harvey-Thompson, S. Patankar, G. C. Burdiak, P. de Grouchy, L. Pickworth, S. J. Stafford, L. Suttle, M. Bennett, S. N. Bland, J. P. Chittenden, G. N. Hall, E. Khoory, R. A. Smith, A. Ciardi, A. Frank, R. E. Madden, K. Wilson-Elliot, and P. Coleman, "Interaction of radiatively cooled plasma jets with neutral gases for laboratory astrophysics studies," High Energy Density Physics **9**, 141–147 (2013).

[22]F. Suzuki-Vidal, S. V. Lebedev, A. Ciardi, L. A. Pickworth, R. Rodriguez, J. M. Gil, G. Espinosa, P. Hartigan, G. F. Swadling, J. Skidmore, G. N. Hall, M. Bennett, S. N. Bland, G. Burdiak, P. De Grouchy, J. Music, L. Suttle, E. Hansen, and A. Frank, "Bow shock fragmentation driven by a thermal instability in laboratory astrophysics experiments," Astrophysical Journal **815**, 96 (2015), arXiv:1509.06538.

[23]G. F. Swadling, S. V. Lebedev, N. Niasse, J. P. Chittenden, G. N. Hall, F. Suzuki-Vidal, G. Burdiak, A. J. Harvey-Thompson, S. N. Bland, P. De Grouchy, E. Khoory, L. Pickworth, J. Skidmore, and L. Suttle, "Oblique shock structures formed during the ablation phase of aluminium wire array z-pinches," Physics of Plasmas **20** (2013).

[24]S. V. Lebedev, L. Suttle, G. F. Swadling, M. Bennett, S. N. Bland, G. C. Burdiak, D. Burgess, J. P. Chittenden, A. Ciardi, A. Clemens, P. De Grouchy, G. N. Hall, J. D. Hare, N. Kalmoni, N. Niasse, S. Patankar, L. Sheng, R. A. Smith, F. Suzuki-Vidal, J. Yuan, A. Frank, E. G. Blackman, and R. P. Drake, "The formation of reverse shocks in magnetized high energy density supersonic plasma flows," Physics of Plasmas **21** (2014).

[25]G. C. Burdiak, S. V. Lebedev, S. N. Bland, T. Clayson, J. Hare, L. Suttle, F. Suzuki-Vidal, D. C. Garcia, J. P. Chittenden, S. Bott-Suzuki, A. Ciardi, A. Frank, and T. S. Lane, "The structure of bow shocks formed by the interaction of pulsed-power driven magnetised plasma flows with conducting obstacles," Physics of Plasmas **24** (2017).

[26]S. C. Bott-Suzuki, L. S. Caballero Bendixsen, S. W. Cordaro, I. C. Blesener, C. L. Hoyt, A. D. Cahill, B. R. Kusse, D. A. Hammer, P. A. Gourdain, C. E. Seyler, J. B. Greenly, J. P. Chittenden, N. Niasse, S. V. Lebedev, and D. J. Ampleford, "Investigation of radiative bow-shocks in magnetically accelerated plasma flows," Physics of Plasmas **22** (2015).

[27]I. H. Mitchell, J. M. Bayley, J. P. Chittenden, J. F. Worley, A. E. Dangor, M. G. Haines, and P. Choi, "A high impedance mega-ampere generator for fiber z-pinch experiments," Review of Scientific Instruments **67**, 1533–1541 (1996).

[28]A. L. Velikovich, I. V. Sokolov, and A. A. Esaulov, "Perfectly conducting incompressible fluid model of a wire array implosion," Physics of Plasmas **9**, 1366 (2002).

[29]R. Drake, *High-Energy-Density Physics. Fundamentals, Inertial Fusion and Experimental Analysis* (2013).

[30]I. H. Hutchinson, *Principles of Plasma Diagnostics* (2002).

[31]J. D. Hare, J. MacDonald, S. N. Bland, J. Dranczewski, J. W. Halliday, S. V. Lebedev, L. G. Suttle, E. R. Tubman, and W. Rozmus, "Two-colour interferometry and Thomson scattering measurements of a plasma gun," Plasma Physics and Controlled Fusion **61** (2019), arXiv:1902.02581.

[32]J. D. Anderson, *Fundamentals of Aerodynamics* (Boston: McGraw-Hill, 2001).

[33]J. P. Goedbloed, R. Keppens, and S. Poedts, *Advanced Magnetohydrodynamics: With Applications to Laboratory and Astrophysical Plasmas* (Cambridge University Press, 2010).

[34]P. K. Kundu, I. M. Cohen, and D. R. Dowling, eds., *Fluid Mechanics (Fifth Edition)*, fifth edition ed. (Academic Press, Boston, 2012) pp. 729–778.

[35]J. D. Hare, L. G. Suttle, S. V. Lebedev, N. F. Loureiro, A. Ciardi, J. P. Chittenden, T. Clayson, S. J. Eardley, C. Garcia, J. W. Halliday, T. Robinson, R. A. Smith, N. Stuart, F. Suzuki-Vidal, and E. R. Tubman, "An experimental platform for pulsed-power driven magnetic reconnection," Physics of Plasmas **25** (2018), arXiv:1711.06534.

[36]S. V. Lebedev, R. Aliaga-Rossel, S. N. Bland, J. P. Chittenden, A. E. Dangor, M. G. Haines, and I. H. Mitchell, "The dynamics of wire array Z-pinch implosions," Physics of Plasmas **6**, 2016–2022 (1999).

[37]S. V. Lebedev, F. N. Beg, S. N. Bland, J. P. Chittenden, A. E. Dangor, M. G. Haines, K. H. Kwek, S. A. Pikuz, and T. A. Shelkovenko, "Effect of discrete wires on the implosion dynamics of wire array Z pinches," Physics of Plasmas **8**, 3734–3747 (2001).